

Submission to: ASCE Journal of Geotechnical and Geoenvironmental Engineering
Article Type: Technical Paper

Title: Axisymmetric Simulations of Cone Penetration in Saturated Clay

Author 1

- Diane M. Moug, Ph.D.
- Assistant Professor; Department of Civil and Environmental Engineering, Portland State University, Portland, OR, 97207, dmoug@pdx.edu.

Author 2

- Ross W. Boulanger, M. ASCE, Ph.D., P.E.
- Professor, Department of Civil and Environmental Engineering, University of California, Davis, CA, 95616, rwboulanger@ucdavis.edu.

Author 3

- Jason T. DeJong, M. ASCE, Ph.D., P.E.
- Professor, Department of Civil and Environmental Engineering, University of California, Davis, CA, 95616, jdejong@ucdavis.edu.

Author 4

- Robert A. Jaeger, Ph.D., P.E.
- Senior Engineer, GEI Consultants Inc., Rancho Cordova, CA, 95670, rjaeger@geiconsultants.com.

Full contact details of corresponding author:

Diane Moug
(503) 7254283
dmoug@pdx.edu

PO Box 761-CEE
Portland, OR 97207-0751

Authors' copy submitted April 2018

Abstract

A direct axisymmetric cone penetration model developed for use with a user-written implementation of the MIT-S1 constitutive model is presented. The penetration model uses the finite difference program FLAC with an Arbitrary Lagrangian Eulerian algorithm that couples FLAC's large deformation Lagrangian formulation with user-written algorithms for rezoning and second-order Eulerian advection remapping. Numerical examples are used to illustrate the performance of the remapping and advection algorithms and cone penetration simulations. Cone penetration at a Boston Blue Clay site is simulated with the Mohr-Coulomb, modified Cam clay, and MIT-S1 constitutive models and compared to measured cone penetration test profiles. Single element simulations illustrate that the MIT-S1 constitutive model captures the significant undrained shear strength anisotropy exhibited by Boston Blue Clay, whereas the modified Cam clay and Mohr-Coulomb models do not. Penetration simulations demonstrate the important effect of undrained shear strength anisotropy on the cone tip resistance, as well as on stress and pore pressure fields around the cone tip and rod.

Introduction

Numerical studies of cone penetration have been performed with direct and indirect models. Direct models simulate penetration with the full axisymmetric cone geometry, but are numerically challenging due to large deformations around the cone. Indirect methods simulate cylindrical or spherical cavity expansion and convert the limit cavity expansion pressures to cone tip resistances using semi-empirical relationships that are significantly different for clays and sands. Direct models offer greater capabilities for examining problems where the cone geometry and full loading condition are important (e.g., layered soils, dissipation tests, partially drained penetration) or where semi-empirical relationships for converting cavity-expansion limit pressures are not established (e.g., intermediate soils including silty/clayey sands).

Nineteen different direct axisymmetric models are summarized in Table 1, including key features of the numerical method (as reported in the references), numerical platform, constitutive models, pore water modeling, and the cone/rod interface condition. Several of the methods, including Teh and Houlsby (1991), Abu-Farsakh et al. (2003), and Ahmadi and Robertson (2005), impose a deformation field around the penetrating cone that is uncoupled from the constitutive soil response. Other methods idealize the contact condition between the cone and soil as frictionless or having low friction in order to limit mesh distortion (Chai et al. 2012, Yi et al. 2012, and Huang et al. 2004). The most common method in Table 1 is an Arbitrary Lagrangian Eulerian (ALE) algorithm, or variants thereof, that couples large Lagrangian deformations with remeshing and remapping steps to overcome the limitations of the other methods described above. Many of the ALE methods used adaptive remeshing techniques that are capable of simulating cone penetration beginning from ground surface by tracking the soil and cone boundaries, and remeshing the grid geometry within these boundaries (Susila and Hryciw 2003, Lu et al. 2004, Walker and Yu 2006,

Liyanapathirana 2009, Walker and Yu 2010, Tolooiyan and Gavin 2011, Kouretzis et al. 2014, Mahmoodzadeh et al. 2014, Aubram et al. 2015, Wang et al. 2015). Several of the methods in Table 1, regardless of numerical procedure, simulate steady cone penetration (i.e., cone penetration at depths sufficiently large that soil self-weight and ground surface boundary effects can be neglected) by modeling a region of soil around the cone along with appropriate far-field boundary conditions (Teh and Houlsby 1991, van den Berg et al. 1996, Abu-Farsakh et al. 1998, Yu et al. 2000, and Abu-Farsakh et al. 2003, and this study).

Most of the direct penetration models listed in Table 1 used relatively simple constitutive models, including Mohr-Coulomb (MC), Tresca, von-Mises, and modified Cam clay (MCC) for undrained penetration in clays, and MC and Drucker-Prager for drained penetration in sand. Two direct penetration models used a more complicated constitutive model for drained penetration in sand; the elastoplastic model for sand by Yao et al. (2004) and the hypoplastic model by Niemunis and Herle (1997). All but one study (Yi et al. 2012) assumed penetration was either perfectly drained (for sand) or perfectly undrained (for clay); several studies for clay further simplified the analysis by assuming uncoupled undrained conditions. The soil constitutive models used for clay in these studies (Table 1) were limited to isotropic or nearly isotropic undrained shear strength behavior and thus cannot simulate the significant undrained shear strength anisotropy observed in most natural soft clays. The effect of undrained shear strength anisotropy on cone penetration in clay was examined by Su and Liao (2002) using an indirect method (a closed form cavity expansion solution), but has not been examined using a direct penetration model to date.

This paper presents a direct axisymmetric cone penetration model for saturated clay using a user-written implementation of the bounding surface plasticity constitutive model MIT-S1 (Pestana and Whittle 1999). This is the first direct penetration model to use a complex bounding surface

constitutive model for clay and the first direct analysis showing the effect of significant undrained shear strength anisotropy on cone penetration. The first section of this paper describes the numerical aspects of the direct axisymmetric penetration model: the geometry and boundary conditions of the penetration model, the mechanics of the finite difference program FLAC (Fast Lagrangian Analysis of Continua; Itasca 2016), and the user-defined ALE scheme including adaptation of the Eulerian remapping scheme for FLAC's mixed discretization scheme, the axisymmetric penetration model geometry, and the MIT-S1 constitutive model. The second section examines numerical performance of the penetration model. First, an example is used to examine how numerical diffusion and dispersion from the ALE algorithm are affected by the rezoning and remapping parameters, including the size of the Lagrangian step before rezoning and Eulerian remapping are performed and the choice of a parameter to limit numerical dispersion. Next, numerical performance of the penetration model is illustrated by sensitivity analyses for one baseline case to show the effects of mesh size, boundary distance, dynamic time-step, and the parameters controlling the ALE algorithm. The last section of this paper presents simulations of cone penetration in a natural deposit of Boston Blue Clay (BBC) in Newbury, Massachusetts using the MIT-S1 and two simpler constitutive models (MC and MCC). Single element simulations for different loading conditions illustrate that the MIT-S1 model is able to capture the undrained shear strength (s_u) anisotropy and strain softening of BBC, whereas the MC and MCC models cannot. The effect of the constitutive model and s_u anisotropy on simulated cone penetration resistance (q_t), stress fields, and excess pore pressure (u) distribution are described. The practical implications for estimating s_u from q_t measurements are discussed, including differences in the derived cone factor (N_{kt}) for different reference strength tests. These analysis results provide the

first measures of validation for the MIT-S1 implementation in FLAC and direct axisymmetric cone penetration model described herein.

Numerical Methods for Cone Penetration Simulations

Cone penetration is simulated with a direct, axisymmetric, steady state method in the finite difference program FLAC. Large deformations around the cone tip and cone shoulder can lead to zone distortion and numerical instability in direct penetration models; these large deformations are addressed with a user-defined ALE algorithm for rezoning and remapping which is described in three parts: the Lagrangian interval, the rezoning step, and the Eulerian remapping interval. This section provides references where the governing equations, theory, and numerical implementation are documented elsewhere; and presents equations when necessary for clarifying implementation details.

Cone Penetration Model Geometry and Boundary Conditions

The axisymmetric model geometry, as shown in Figure 1, was developed to simulate steady state penetration at depths sufficiently large that self-weight and ground surface effects can be neglected. The cone diameter is 3.57 cm (standard 10-cm² cone area). The model extends 22.5 cone diameters below the cone tip, 5 cone diameters above the cone shoulder, and 22.5 cone diameters to the radial boundary. The model is highly discretized near the cone face where deformation concentrates; zone sizes increase with distance from the cone face based on a power distribution.

The analysis begins with a “wished-in-place” cone at the depth of interest, followed by sufficient cone penetration to produce steady distributions of stresses and pore pressure throughout the mesh. The boundary conditions are specified for simulating soil flowing upwards relative to a stationary cone; soil conceptually flows into the bottom of the model and exits at the top of the model

(Figure 1). Penetration velocity is applied to gridpoints at the top boundary, which assumes that the soil node adjacent to the rod is sliding relative to the rod at this location. The in-situ vertical stress condition is applied at the bottom boundary. The right radial boundary is represented with interface elements that approximate an infinite elastic boundary condition.

The fixed-in-place cone tip and shaft are connected to the adjacent soil zones by interface elements whose shear strength is governed by a Mohr-Coulomb friction criterion. The ratio of the interface friction angle (ϕ_{cone}) to the soil's critical state friction angle (ϕ'_{cs}) is $\delta = \phi_{cone}/\phi'_{cs}$. The axisymmetric boundary condition does not allow gridpoints at $x = 0$ to displace in the x-direction. Therefore, the soil node connected to the cone tip is fixed in the x-direction (i.e., cannot slide up the face) and constrained to move vertically (due to the interface elements being relatively rigid in the normal direction). This approximation of deformation conditions at the cone tip was judged to be reasonable for the current model geometry as the solutions were found to be insensitive to further refinements in the discretization; this finding is attributed to the already small zone sizes at the cone tip and the observation that the soil zones near the cone tip all go to critical state conditions during cone penetration. The other soil gridpoints along the cone face and shaft can deform parallel to the cone and shaft boundaries. The gridpoint at the cone shoulder is connected to an interface element along the rod and not to an interface element on the cone face (otherwise, the normal stiffness of two angled interface elements would lock the node against movement). This configuration means the soil zone immediately below the cone shoulder will penetrate the cone by a small amount during Lagrangian deformation. Alternatively, the gridpoint at the cone shoulder could be connected to an interface element on the cone face, which would result in the soil zone immediately above the cone shoulder expanding radially (analogous to opening of a small gap behind the shoulder) during Lagrangian deformation. The steady solutions were not sensitive

to either approach, which is attributed to the small size of these zones and the use of small intervals of Lagrangian deformation as discussed later.

Consistent with the cone penetration models presented in Table 1, this model does not directly address shear bands and strain localizations in the continuum elements, even though development of periodic (in space and time) shear bands around penetrometers in clay are a known phenomenon (e.g., Zhou and Randolph 2007). The MIT-S1 constitutive model can address large deformations and accommodate a strain-softening and localization response; however, this steady state penetration solution did not produce shear bands or strain localizations in the continuum elements, possibly because of the steady state solution technique. The Mohr-Coulomb interface elements do provide an approximate accounting for strain localization along the soil-cone tip and shaft interfaces.

Large deformations of the model geometry will concentrate around the cone tip and cone shoulder, which can lead to numerical instability and mesh entanglement if the Lagrangian interval is too large. Large deformations are accommodated with an ALE algorithm that performs grid rezoning and model property remapping operations throughout simulated penetration. Implementation and evaluation of the ALE algorithm are described in later sections.

FLAC Finite Difference Analysis

FLAC is an explicit finite difference program for geotechnical engineering analysis. The global governing equations and their numerical implementation are described in Itasca (2016). This section provides an overview of those numerical aspects that are important for the cone penetration model described herein, including: (1) the explicit formulation and how it relates to the performance of the numerical formulations and the constitutive models, (2) the large deformation

Lagrangian analysis and how it relates to the user-written ALE algorithm, and (3) the mixed discretization and how it relates to the user-written remapping of zone variables.

FLAC's explicit computational cycle is illustrated in Figure 2. The penetration model described in the previous section uses FLAC's dynamic analysis to step towards steady-state penetration conditions from the initial wished-in-place conditions. The maximum dynamic time-step is internally constrained by the speed information travels across model zones, which depends on zone dimensions, material wave velocities, damping parameters, and pore fluid permeability. For example, in the baseline case of simulated penetration presented later, the maximum dynamic time step was 1.1×10^{-6} seconds and the cone velocity (relative to the soil mesh) was 0.20 m/s (which reached undrained steady state penetration conditions faster than the standard penetration rate of 0.02 m/s with no observed effect on results), which means that over 10^5 calculation steps were performed per simulated cone diameter of penetration.

FLAC calculates equivalent nodal (gridpoint) forces from stresses in subzones. The FLAC grid is composed of quadrilateral zones, which are discretized into two overlying sets of two constant-strain, triangular subzones. A mixed discretization scheme is used to prevent "hourglass" zone deformations (Marti and Cundall, 1982) wherein the isotropic components of stress and strain are the same for all subzones, while deviatoric components are treated separately for each subzone. Mechanical deformation in FLAC is governed by the equation of motion, with gridpoint accelerations computed from lumped masses and unbalanced forces. Gridpoint velocities are used to calculate each subzone's strain rate and strain increments. Gridpoint and material coordinates are updated in FLAC's large deformation mode from the calculated displacements, and the user-implemented rezoning and remapping steps of the ALE algorithm are called after a user-specified amount of zone geometry deformation. Subzone stresses are constitutively calculated from the

strain increments, and the cycle is repeated. During remapping operations, values calculated at the subzone level must be remapped for each subzone. Pore pressures in FLAC are located at gridpoints and develop from either fluid flow (governed by Darcy's law) or mechanical volumetric strain (governed by Biot theory); therefore, gridpoint values must be remapped in addition to zone and subzone values.

FLAC's constitutive model library includes the MC and MCC soil models and it allows for interfacing with user-defined constitutive models such as the MIT-S1 model used in this paper. In addition, FLAC includes its own scripting language that enables implementation of user-defined numerical procedures, such as the rezoning and remapping operations described in the following section.

ALE Algorithm for Direct CPT Simulations in FLAC

The Arbitrary Lagrangian Eulerian (ALE) algorithm implemented in this study couples FLAC's large deformation Lagrangian formulation with user-defined routines for both rezoning and Eulerian remapping steps. Coupling the Lagrangian deformation with a rezoning and remapping step allows penetration to be simulated to steady-state conditions without the severe zone deformation, mesh entanglement, and numerical instability that occurs with solely a Lagrangian method. User-defined modules for rezoning and Eulerian remapping were required because FLAC's current rezoning algorithm is limited to plane strain conditions. Only those equations and concepts necessary to describe the adaptations made for FLAC or for background to the sensitivity studies in the following section are presented here. The full equations for the rezoning step and Eulerian remapping step are found in Pember and Anderson (2001) and Moug (2017). The numerical implementation of this ALE algorithm for FLAC is summarized as a pseudo-code in the Appendix of this paper. Moug (2017) includes an example implementation of the cone penetration

model along with the full ALE code for use with FLAC. The Lagrangian interval, rezoning step, and Eulerian intervals are briefly described below.

Lagrangian Interval

A dynamic time interval (or specified number of explicit time steps) in FLAC's large deformation mode simulates a Lagrangian interval of penetration. The time interval and cone penetration velocity together determine how much cone penetration is simulated in this Lagrangian interval. The amount of deformation during the Lagrangian interval must be limited such that significant overlap remains between the deformed and remapped model zones, as illustrated later in the verification examples.

Rezoning Step

In the rezoning step, the grid coordinates are mapped to a new rezoned geometry while material coordinates remain stationary. ALE algorithms might use adaptive remeshing where the rezoned geometry adapts to changing boundaries and is refined in large deformation areas. Adaptive remeshing was not necessary for the present study, so the rezoned geometry is instead taken as the original "undeformed" geometry. Thus, the algorithm is net Eulerian where soil material moves relative to a stationary cone and grid. Similar net Eulerian methods for geotechnical penetration problems were presented in Liyanapathirana et al. (2000) and van den Berg et al. (1996).

The remapping and Eulerian rezoning methods reference model values in both space and pseudo-time (i.e. advection time). Model geometry is transformed to general quadrilateral coordinates $(\xi, \eta) = (i, j)$ as shown in Figure 3. Model zones are referenced as i, j ; η edges are referenced as $i \pm 1/2$; ξ edges are referenced as $i, j \pm 1/2$, and gridpoints are referenced as $i \pm 1/2, j \pm 1/2$. The rezoning step and subsequent Eulerian advection remapping step occur over a pseudo time-step with duration t_f . At $t = 0$ the Lagrangian interval has finished and the geometry is in a

deformed state with coordinates \mathbf{X}^n . At $t = t_f$ the geometry has been advected to the undeformed state with coordinates \mathbf{X}^{n+1} .

Calculation and storage of undeformed zone volumes (σ_{ij}^{n+1}) from gridpoint coordinates are required at model initialization. Pember and Anderson (2001) provide volume equations assuming two-dimensional plane strain geometry, therefore volume calculations were adapted for implementation with the axisymmetric cone model.

The Pember and Anderson (2001) implementation was extended for remapping FLAC model variables that are located at gridpoints such as pore pressure. The adaptation treats gridpoints as the center of pseudo-zones which have corners located at zone centers and are connected by pseudo-edges as shown in Figure 4. Therefore, all gridpoint, edge, and zone calculations performed in the rezoning step should be performed for model zones and the pseudo-zones around gridpoints.

Eulerian (Remapping) Interval

The Eulerian interval advects material and field properties from \mathbf{X}^n to \mathbf{X}^{n+1} over the same time-step, t_f , as in the rezoning interval. Zone density (ρ_{ij}) is the first model property remapped because ρ_{ij}^{n+1} is required for remapping all other model zone and gridpoint properties, which are generalized as w_{ij} . The remapped model zone properties include yield surface variables, plastic potential variables, and stress components. For the MIT-S1 model, this corresponds to remapping 40 variables per model zone (10 variables per subzone) plus the pore pressure for each gridpoint. ρ_{ij}^{n+1} values are calculated by (1) computing axisymmetric volume fluxes between \mathbf{X}^n to \mathbf{X}^{n+1} at all edges (e.g. $\delta\sigma_{i,j\pm 1/2}$, $\delta\sigma_{i\pm 1/2,j}$) as shown in Figure 5, (2) computing σ_{ij}^n from σ_{ij}^{n+1} values stored at initialization and $\delta\sigma$ values, (3) computing the mass in the deformed zone (M_{ij}^n) from ρ_{ij}^n and σ_{ij}^n , (4) estimating density values at edges at $t = t_f/2$ (e.g. $\rho_{i,j\pm 1/2}^{n+1/2}$, $\rho_{i\pm 1/2,j}^{n+1/2}$) with the corner

transport upwind method (Colella 1990), (5) estimating mass fluxes at each edge (e.g. $F_{i,j\pm 1/2}, F_{i\pm 1/2,j}$) from $\delta\sigma$ and $\rho^{n+1/2}$ edge values, and finally (6) estimating ρ_{ij}^{n+1} :

$$\rho_{ij}^{n+1} = \frac{M_{ij}^{n+1}}{\sigma_{ij}^{n+1}} = \frac{M_{ij}^n + (F_{i-1/2,j} - F_{i+1/2,j}) + (F_{i,j-1/2} - F_{i,j+1/2})}{\sigma_{ij}^{n+1}} \quad (1)$$

All w_{ij} values are remapped in a similar manner to ρ_{ij} values. The corner transport upwind method is also used to estimate w_{ij} values at edges at $t = t_f/2$. Remapped zone values are estimated as:

$$w_{ij}^{n+1} M_{ij}^{n+1} = w_{ij}^n M_{ij}^n + \left(w_{i-1/2,j}^{n+1/2} F_{i-1/2,j} - w_{i+1/2,j}^{n+1/2} F_{i+1/2,j} \right) + \left(w_{i,j-1/2}^{n+1/2} F_{i,j-1/2} - w_{i,j+1/2}^{n+1/2} F_{i,j+1/2} \right) \quad (2)$$

Model and kinematic properties in FLAC are located at either quadrilateral zones, triangular subzones, or gridpoints. Remapping for subzone properties is performed similar to properties located in the quadrilateral zone, with edge values and fluxes estimated for quadrilateral edges but based on property values from subzones. The procedure for remapping gridpoint values in FLAC is similar to that for the zone values in Equation 2 with edges around gridpoints treated as pseudo-edges as shown in Figure 5. Mass fluxes at pseudo-edges are approximated as the axisymmetric volume-weighted average between the adjacent four parallel edges.

Slopes of remapped properties in the ξ and η directions ($\Delta_{\xi} w_{ij}$ and $\Delta_{\eta} w_{ij}$, respectively) across the i, j zone or gridpoint are required to estimate property gradients and edge values of remapped properties. Slopes are estimated with van Leer limited monotonic central differences (van Leer, 1979) and are described to support the numerical evaluation work presented in the following section. The van Leer limiters will estimate slopes less than or equal to the average of adjacent zones, and the central difference is set to zero if the slope changes directions across neighboring zones. The van Leer limited central difference in the ξ direction (Δw^{ξ}) and ξ gradient (w_{ξ}) are computed as,

$$\Delta_C w_{ij}^{\xi} = 0.5(w_{i+1,j} - w_{i-1,j})$$

$$\Delta_R w_{ij}^\xi = w_{i+1,j} - w_{i,j}$$

$$\Delta_L w_{ij}^\xi = w_{i,j} - w_{i-1,j}$$

$$\text{if } \Delta_L w \Delta_R w > 0,$$

$$\Delta_\xi w_{ij} = \min \left(\left| \Delta_C w_{ij}^\xi \right|, \omega_L \left| \Delta_R w_{ij}^\xi \right|, \omega_L \left| \Delta_L w_{ij}^\xi \right| \right) * \text{sign}(\Delta_C w_{ij}^\xi)$$

else

$$\Delta_\xi w_{ij} = 0$$

$$w_\xi = \frac{\Delta_\xi w}{\Delta \xi} \tag{3}$$

The van Leer limited central difference and gradient in the η direction are computed similarly.

The van Leer limiting factor (ω_L) should fall between 1 and 2 for a second-order algorithm where ω_L can be a function of the overlapping distance between a deformed and undeformed zone. Large remapping distances will require stronger limiting, which is achieved with ω_L close to 1, to prevent numerical dispersion. If ω_L is set at 0, the algorithm becomes first-order accurate. A value of $\omega_L = 1$ was found to work well for the present study; results for values of 0, 1, and 2 are compared later in a verification example.

After remapped model zone and gridpoint properties have been determined and assigned to the undeformed model geometry, the constitutive model may initially violate plastic consistency (e.g., stress conditions may lie outside the yield surface). This is corrected at the element level, where the constitutive model must iterate back to the plastic yield surface in the same manner that the constitutive model performs implicit integration throughout Lagrangian analysis. Details of the iterative forward-Euler integration scheme in our implementation of MIT-S1 with FLAC are available in Jaeger (2012).

Assessment of Numerical Methods

The user-defined ALE algorithm and axisymmetric cone penetration model were evaluated through numerical exercises, as described in this section. Numerical dispersion and diffusion from repeated rezoning and remapping cycles are evaluated first, followed by a sensitivity study of the cone penetration model to numerical aspects of the solution procedure.

Performance of Rezoning and Remapping Algorithms

Numerical diffusion and dispersion due to the rezoning and remapping cycles of the ALE algorithm is illustrated using the example shown in Figure 6a, which is similar to the example by Dukowicz and Kodis (1987). This example involves advecting an initially discontinuous distribution of a property (shown in Figure 6a) from the bottom to the top of a mesh, which in this case is similar to the mesh used in cone penetration modeling (e.g., Figure 1) but with equally sized zones. The Lagrangian interval applies rigid vertical displacement to the model, therefore this example does not solve the constitutive equations or penetration process, but rather just tests the numerical diffusion and dispersion due to the rezoning and remapping cycles. Numerical diffusion will be evident by numerical smoothing of the initially discontinuous property distribution as it advects through the mesh, whereas numerical dispersion will be evident by remapped values exceeding the distribution's initial limits.

The dependence of numerical diffusion and dispersion on the limiting factor ω_L (Equation 3) and the size of Lagrangian interval are illustrated in Figures 6b-g. Results for $\omega_L = 0, 1, \text{ and } 2$ with a Lagrangian interval displacement of 1.9 mm (0.2 times the minimum zone height) are shown in Figures 6b, 6c, and 6d, respectively. Results for the same ω_L values but with a Lagrangian interval displacement only $1/10^{\text{th}}$ as large (0.02 times the minimum zone height) are shown in Figures 6e, 6f, and 6g, respectively. The total number of remapping steps was 500 with the larger Lagrangian

interval (Figures 6b-6d) and 5,000 with the smaller Lagrangian interval (Figures 6e-6g). Numerical diffusion is greatest when $\omega_L = 0$ (i.e., the algorithm is first-order) for either Lagrangian interval size (Figures 6b and 6e). Numerical diffusion is reduced when $\omega_L = 1$ for either case, although diffusion is greater for the smaller Lagrangian interval (Figure 6f versus 6c) because it requires ten times more remapping steps. Numerical diffusion is further reduced when $\omega_L = 2$, but it is accompanied by dispersion (property values outside the initial distribution limits) for the larger Lagrangian interval (Figure 6d). This example demonstrates that the second-order algorithm ($\omega_L = 1$ or 2) will decrease numerical diffusion due to remapping when compared to a first-order algorithm, but that stronger limiting (e.g., $\omega_L = 1$) may be required with large Lagrangian intervals to avoid numerical dispersion.

Evaluation of Numerical Modeling Procedures for Cone Penetration

A series of direct cone penetration analyses were performed to evaluate sensitivity of the solutions to the numerical aspects of the model, including mesh geometry, zone size, van Leer limiting factors, Lagrangian interval size, and dynamic time-step. Results are compared in terms of q_t versus penetration distance in Figure 7 for a baseline case with the MCC constitutive model calibrated to BBC data (Table 2), a perfectly smooth ($\delta = 0$) cone face and rod, and an isotropic hydraulic conductivity of 1×10^{-8} m/s.

The effect of model zone size near the cone face is shown in Figure 7a. Essentially the same solution is obtained if the minimum zone height against the cone face is 0.03 or 0.06 (baseline case value) times the cone diameter; this corresponds to 19 and 10 zones in contact with the cone face, respectively. The solution begins to differ and show oscillations if the minimum zone height is increased to 0.12 times the cone diameter (only 5 zones in contact with the cone face) and is poor

with significant oscillations if it is increased to 0.19 times the cone diameter (i.e., only 3 zones in contact with the cone face).

The effect of distance to the right and bottom boundaries, which were kept equal to each other, is shown in Figure 7b. Essentially the same solution is obtained if these distances are 45 or 90 cone diameters. The q_t is increased by about 1%, 2.5%, and 7.5% if these distances are reduced to 22.5 (baseline case value), 11.2, and 5.6 cone diameters, respectively.

The effect of setting the van Leer central difference limiting factor ω_L equal to 0 (first order), 1, or 2 was also examined. The simulated penetration resistances were unaffected (less than 0.20% difference); similarly, stress and pore pressure fields did not show notable differences throughout simulated penetration. Notable differences were likely not observed between different ω_L values because the problem approaches the same steady state stress conditions. However, for the more complex MIT-S1 constitutive model, the higher order values for ω_L did reduce numerical noise for spatial solutions (contour plots) with some numerical parameter combinations, but also did not significantly affect the steady state solution for the more stable parameter combinations. Penetration simulations in this paper use $\omega_L = 1$ and the Lagrangian deformation limited to half the minimum zone size. As demonstrated in Figure 6, large remapping distances relative to zone size require stronger limiting to prevent numerical dispersion.

The effect of the Lagrangian interval's penetration distance is shown in Figure 7d. The baseline case is 1.7 mm of cone penetration per Lagrangian interval, corresponding to 0.50 times the minimum zone height in the mesh (i.e. at the cone face). The two smaller Lagrangian intervals (0.25 and 0.10 times the minimum zone height) shows similar results to the baseline case. However, the largest Lagrangian interval (0.75 times the minimum zone height) resulted in numerical instability after penetrating a distance of only 3 cone diameters.

The effect of reducing the dynamic time step below the default (baseline case) did not affect the penetration resistance. The solutions were essentially the same using 1.0, 0.5, or 0.25 times the default (maximum) time step (1.1×10^{-6} seconds for this problem).

The results summarized in Figure 7 provide a measure of verification for the numerical modeling procedures in two ways. First, they indicate that reasonable variations in the numerical analysis parameters, within certain bounds, do not have significant effects on the simulated q_t . Second, the q_t for the baseline case is consistent with values obtained by others using MCC models in direct penetration modeling. The relationship between q_t and s_u is often expressed using the form,

$$q_t = \sigma_{vo} + N_{kt}s_u \quad (4)$$

where N_{kt} is a cone bearing factor that depends on the type of test for which s_u is estimated. The baseline case corresponds to $N_{kt} = 9.2$ for a K_o normally consolidated undrained triaxial compression $s_u = 30$ kPa, $\sigma'_{vo} = 100$ kPa, and an elastic shear modulus (G) equal to 75 times s_u . This value of N_{kt} is in good agreement with $N_{kt} = 9$ reported by Yu et al. (2000) using an MCC model with a similar G/s_u ratio and interface roughness condition. Additional analyses for other values of s_u , G/s_u , and K_o produced results in good agreement with those reported by Yu et al. (2000), indicating that the penetration model is producing reasonable results with this constitutive model.

Penetration in Boston Blue Clay

The penetration model was used with the MC, MCC, and MIT-S1 constitutive models to simulate steady-state penetration in BBC at a site in Newbury, Massachusetts (Landon 2007). The MC and MCC models are included within the FLAC library of soil models. MIT-S1 was implemented in FLAC as a user-defined constitutive model by Jaeger (2012). The following sections summarize s_u data for BBC loaded in triaxial compression, direct simple shear, and triaxial extension, the

responses of the three constitutive models in single element simulations for these test paths, and the results of cone penetration simulations using the three constitutive models.

Undrained Strengths of Boston Blue Clay

Laboratory test results on intact and resedimented BBC samples are summarized in Table 3 for K_o consolidated undrained triaxial compression (CK_oUC), K_o consolidated undrained triaxial extension (CK_oUE), and K_o consolidated undrained direct simple shear (CK_oUDSS) loading conditions. Under normally consolidated conditions the ratio of s_u to the initial vertical effective stress (s_u/σ'_{vo}) for CK_oUC loading is about 0.28 and 0.33 for intact and resedimented specimens, respectively. The s_u/σ'_{vo} for CK_oUDSS and CK_oUE loading decreases to 0.14 and 0.20, respectively, for resedimented specimens (data are not available for intact specimens). For an overconsolidation ratio (OCR) of 2.0, the s_u/σ'_{vo} for CK_oUC loading is about 0.42 and 0.54 for intact and resedimented specimens, respectively, with the s_u/σ'_{vo} decreasing to 0.28 and 0.31 for CK_oUE loading for intact and resedimented specimens, respectively. These differences in s_u for different test types are consistent with ranges reported for other sedimentary clays (Kulhawy and Mayne 1990); e.g., the s_u for CK_oUE loading is 42-67% of the s_u for CK_oUC loading depending on the sample type and OCR.

Calibration and Constitutive Behavior

The MIT-S1 calibration for BBC, as presented in Table 4, uses the parameter values from Jaeger (2012) with slight modifications; e.g., the C_b value was increased from 540 to 850 to achieve the in-situ shear velocity of BBC reported in Landon (2007). The s_u/σ'_{vo} from single element simulations at OCRs of 1.0, 2.0, and 2.2 for CK_oUC, CK_oUE, and CK_oUDSS loading conditions are summarized in Table 3. This calibration produces peak s_u/σ'_{vo} values of 0.32, 0.18, and 0.17

for normally consolidated CK_oUC, CK_oUE and CK_oUDSS loading conditions, respectively, which are reasonable approximations of the experimentally observed s_u anisotropy.

The MCC calibration follows the Randolph (1979) calibration as summarized in Table 2, except K_o was changed from 0.55 to 0.49 to match the MIT-S1 calibration. This calibration produces a s_u/σ'_{vo} of 0.30 for both normally consolidated CK_oUC and CK_oUE loading conditions and a s_u/σ'_{vo} of 0.34 for normally consolidated CK_oUDSS loading (Table 3).

The MC calibration for undrained loading involved setting the friction angle (ϕ) to zero and the soil cohesion equal to the target s_u value. For the purpose of this study, the target s_u and elastic shear moduli were set equal to that for the MCC calibration. For $\phi = 0$, the strength envelope of the MC model reduces to the Tresca failure criterion and produces the same peak s_u/σ'_{vo} of 0.30 for all loading conditions (Table 3).

Figure 8 shows the BBC K_o normally consolidated yield surfaces for MC, MCC, and MIT-S1 where $\sigma'_{vo} = 100 \text{ kPa}$. The ability of MIT-S1 to approximate s_u anisotropy stems from incorporation of the Matsuoka-Nakai (1974) generalization of the yield and critical state surfaces, and from incorporation of an anisotropy tensor in the yield surface expression. Figure 8 demonstrates the isotropic yield surfaces for MC and MCC models, which are consistent with the s_u values predicted in the CK_oUC and CK_oUE simulations.

Stress and excess pore pressure (u) versus strain as well as stress path responses from single element simulations with normally consolidated BBC calibrations are shown in Figure 9 to illustrate the different behaviors between the three constitutive models. The initial σ'_{vo} and σ_{vo} were 100 kPa and K_o was set equal to 0.49. The stress-strain responses for CK_oUC loading conditions (the solid lines in Figure 9a) show similar s_u values for the three soil models, which was one objective of the calibration process. Only the MIT-S1 model shows post-peak strain softening

behavior, which was observed in normally consolidated CKoUC testing on block samples of BBC by Landon (2007), and on resedimented samples of BBC by Pestana et al. (2002). The stress-strain responses for CKoUE (the dashed lines in Figure 9a) and CKoUDSS (the solid lines in Figure 9d) illustrate how these calibrations for the MC and MCC models result in significant overestimations of s_u for these loading conditions. The u responses in Figure 9 illustrate the significant differences in shear-induced u for the three constitutive models. The MC model, with $\phi = 0$ and associative flow, only develops u in response to changes in mean total stress (p), which is why MC generates the smallest u for all three loading conditions (Figures 9b and 9e). The MCC model generates significantly greater u than the MC model for all three loading conditions because the MCC model develops plastic volumetric strains once the yield surface has been reached and the MC model does not. The MIT-S1 model generates even greater u for all three loading paths because the model's bounding surface was calibrated to produce more realistic approximations of BBC stress paths and s_u anisotropy. The greater generation of u for the MIT-S1 model is evident in its stress paths moving to significantly lower effective stresses during shearing than for either the MC or MCC models (Figures 9c and 9f). Pestana and Whittle (1999) and Pestana et al. (2002) compared experimental results for resedimented BBC to the MIT-S1 constitutive response to show that MIT-S1 captures the observed experimental soil behavior in CKoUC, CKoUE, and CKoUDSS loading paths across a range of overconsolidation ratios.

Simulated Cone Tip Resistance

The penetration model was first used to simulate steady-state penetration in BBC at the Newbury site at a depth of 9.6 m where $\sigma'_{vo} = 100$ kPa and the OCR = 2.2, the groundwater level was at a depth of 1.7 m (Landon 2007). The interface roughness condition was $\delta = 0.8$. The isotropic hydraulic conductivity is 1×10^{-8} m/s for all Newbury site penetration models in this paper, which

is small enough that undrained penetration conditions prevail and an anisotropic hydraulic conductivity (where hydraulic conductivity is lower than 1×10^{-8} m/s in the vertical direction) does not impact the solution. The differences in q_t , stress fields, and u fields around the cone for the three constitutive models are described and related to the differences in the constitutive responses exhibited in the single element simulations.

The simulated q_t versus penetration distance for all three constitutive models are presented in Figure 10. Steady-state q_t values were reached by 2 to 6 cone diameters of penetration, but penetration was simulated to 25 cone diameters to produce steady state stress conditions along the cone shaft.

The simulated q_t with the MC and MCC models were 750 kPa and 735 kPa, respectively. This similarity in q_t values is expected because the two models produce essentially the same s_u of 59 kPa for CK_oUC and CK_oUE loading conditions. These simulations, with their essentially isotropic s_u values, correspond to an $N_{kt,ISO}$ of about 9.7 for MC and 9.5 for MCC. The subscript ISO emphasizes that bearing factors derived for these types of models are based on approximately isotropic undrained shear strengths.

The simulated q_t with the MIT-S1 model is about 536 kPa, about 30% smaller than with the MC and MCC models. The smaller q_t value with the MIT-S1 model is expected because soil is sheared in various modes during cone penetration (Baligh 1985), and the MIT-S1 model produces lower s_u values for all but the CK_oUC loading condition; i.e., MIT-S1 with OCR of 2.2 and σ'_{vo} of 100 kPa produces s_u of 54, 38, and 36 kPa for CK_oUC, CK_oUE and CK_oDSS loading conditions respectively. This simulation result corresponds to $N_{kt,C}$, $N_{kt,E}$ and $N_{kt,DSS}$ values of 6.7, 9.5 and 10.0, respectively.

The complex loading paths of soil near a penetrating cone do not correspond closely to any single laboratory element test, but rather represent a combination of compression, simple shear, and extension paths (Baligh 1985). For penetration with the MIT-S1 model, the q_t could alternatively be related to the average s_u for these three test types (i.e., 39.3 kPa for this example) which would correspond to a $N_{kt,ave} = 8.7$. This value is, however, smaller than the $N_{kt,ISO}$ obtained with the MC and MCC models. These results illustrate that N_{kt} values are significantly affected by s_u anisotropy and are unique to the specific reference strength test against which they are determined. The simulated q_t values, now including results for a depth of 5.6 m where the OCR = 4.3, are plotted with CPT profiles from the Newbury site in Figure 11 after Landon (2007). The CPT1 and CPT2 profiles were located approximately 10 m apart. The measured q_t at CPT2 were about 20-30% greater than at CPT1 over the depths of interest. The Sherbrooke block sample that was used to obtain the intact CKoUC s_u value in Table 3 was located approximately 4 m west of CPT2 and 7.5 m south of CPT1. Simulations with the MCC and MC models produced q_t values that are close to, or slightly above, the values measured in CPT2, whereas simulations with the MIT-S1 model produced q_t values that are closer to those measured in CPT1. The MCC and MC models produced larger q_t values because they were calibrated to the stronger CKoUC loading condition (Table 3). Simulations with the MIT-S1 model produced lower q_t values because its calibration accounts for lower s_u values for loading paths more analogous to extension or simple shear loading. For this site, the spatial variation in q_t values between CPT1 and CPT2 are as large as the differences in the q_t values simulated using these three models.

The N_{kt} values from these simulations were also compared to typical N_{kt} values in geotechnical engineering practice and N_{kt} values determined analytically. Typical N_{kt} values used in geotechnical engineering vary between 15 and 30 (Fleming et al. 2009) which reflects a range of

site specific factors including soil stiffness, cone and sleeve roughness, s_u anisotropy, and soil sensitivity (Schneider et al. 2008). Lunne et al. (2003) reported N_{kt} values of 6-15 for Onsoy clay based on s_u values from high-quality block samples, and noted that higher N_{kt} values in some field studies may be attributed to lower s_u values caused by greater sample disturbance when not using high quality block samples. Lu et al. (2004) simulated penetration with a MC model and reported an N_{kt} value of 9.7 for similar penetration conditions as described in this section.

Simulated Stress Fields

The simulated mean total stress fields (p) around the penetrating cone after 25 cone diameters of penetration are shown in Figure 12 for each soil model at a depth of 9.6 m. The steady-state p distributions show similar values in the cone tip area for the MC and MCC models, whereas p is less for the MIT-S1 model. The differences in p are consistent with the differences in q_t for the three models.

Simulated Pore Pressure Fields

Steady-state u fields are presented in Figure 13 for the three constitutive models. There are two components to the u generated during undrained cone penetration: (1) due to an increment in p , and (2) due to an increment in deviatoric stress or strain. Penetration-induced u with the MC model are slightly smaller than with the MCC soil model. The p fields are similar for the two models because they have similar strength behaviors and therefore produce similar q_t . The MC model, however, generates less u during deviatoric shearing as illustrated by the single element simulations in Figure 9, and thus has slightly smaller values of u around the penetrating cone.

The steady-state u for the MIT-S1 model shows smaller u near the cone face compared to either the MC or MCC models, but greater u for some zones near the cone shaft above the tip. The smaller values near the cone face are attributed to the MIT-S1 model producing smaller p and q_t because

of its lower average strength. The u near the cone shaft above the tip are larger with MIT-S1 because it produces more u during deviatoric shearing (as shown in Figure 9) and the p for the three models are not as different in this area.

Conclusions

A direct axisymmetric cone penetration model was developed for use with a user-written implementation of the MIT-S1 constitutive model (Pestana and Whittle 1999) in the finite difference program FLAC (Itasca 2016). The cone penetration model uses an ALE algorithm that couples FLAC's large deformation Lagrangian formulation with user-written algorithms for rezoning and remapping with a second-order, mass-conservative, Eulerian upwinding technique after Colella (1990). The current application to steady penetration involved remapping to the original geometry, such that the solution is net Eulerian. Results of sensitivity analyses indicate that the ALE algorithm and cone penetration model are reasonably robust.

Cone penetration at a Boston Blue Clay site was simulated using the Mohr-Coulomb, modified Cam clay, and MIT-S1 constitutive models. Single element simulations illustrated that the MIT-S1 constitutive model is capable of simulating the s_u anisotropy and strain softening exhibited by BBC in undrained triaxial compression, undrained triaxial extension, and undrained direct simple shear, whereas the modified Cam clay and Mohr-Coulomb models cannot. Cone penetration simulations illustrated the important effect of s_u anisotropy on q_t and associated N_{kt} factors, as well as on stress and u fields around the cone tip and rod. The simulated q_t were in reasonable agreement with measured values.

Appendix

The implementation of an Arbitrary Lagrangian Eulerian algorithm for axisymmetric geometry is summarized as a pseudo-code having four main components: initialization, Lagrangian interval,

rezoning step, and Eulerian interval. This implementation is fully detailed in Pember and Anderson (2001); for consistency, the same symbolic conventions are used in this paper. Symbols are defined in the List of Notation. The edge value estimation in the Eulerian interval is based on the corner transport upwind method (Colella 1990) with direction gradients estimated with van Leer central difference limiters (van Leer 1979). This pseudo-code is presented for remapping model zone values, a similar procedure is used for remapping values located at gridpoints and subzones. The full code for use with FLAC is available in Moug (2017).

Initialization

1. Calculate and store:
 - i. Undeformed gridpoint and coordinates: $\mathbf{X}_{ij}^{n+1} = (x_{ij}, y_{ij})$
 - ii. Undeformed axisymmetric zone volumes: σ_{ij}^{n+1}

Lagrangian Interval

2. Run FLAC in large deformation mode for a Lagrangian interval
3. Store deformed grid coordinates: $\mathbf{X}_{ij}^n = (x_{ij}, y_{ij})$

Rezoning Step

4. Calculate and store:
 - i. Gridpoint rezoning velocities: $\mathbf{s} = \frac{\mathbf{x}^{n+1} - \mathbf{x}^n}{t_f}$
 - ii. Deformed edge lengths: $\Delta\eta_{i+1/2,j}, \Delta\xi_{i,j+1/2}$
 - iii. Deformed edge normal vectors: $\mathbf{n}_{i,j+1/2}^\eta, \mathbf{n}_{i+1/2,j}^\xi$
 - iv. Deformed zone Jacobians: J_{ij}
5. Set grid geometry to undeformed geometry: $x_{ij} = x_{ij}^{n+1}, y_{ij} = y_{ij}^{n+1}$

Eulerian Interval

6. Calculate axisymmetric transport volumes between \mathbf{X}_{ij}^n and \mathbf{X}_{ij}^{n+1} at all edges: $\delta\sigma_{i\pm 1/2,j}$, $\delta\sigma_{i,j\pm 1/2}$
7. Calculate volume fluxes between deformed grid and rezoned grid at all edges: $Q_{i\pm 1/2,j}$, $Q_{i,j\pm 1/2}$
8. Calculate remapped model values at all zone edges at $t = t_f/2$ with the corner transport upwind (Colella 1990) method:
 - i. Estimate and store van Leer limited central differences (van Leer, 1979) for each remapped property in ξ and η directions for every zone (Equation 3): $\Delta_\xi w_{ij}$, $\Delta_\eta w_{ij}$
 - ii. Estimate and store ξ and η gradients for each remapped property: w_ξ , w_η
 - iii. Determine edge state to be estimated for each edge by upwinding with $\delta\sigma$ values
 - iv. Estimate remapped property values for ξ and η edges at $t = t_f/2$
 - a. Calculate cross-transport gradient at ξ and η edges: w_{p_η} , w_{p_ξ}
 - b. Calculate ξ and η edge values for state found in 8.iii.a: $w_{i\pm 1/2,j}^{n+1/2}$, $w_{i,j\pm 1/2}^{n+1/2}$
9. Calculate remapped zone density:
 - i. Calculate deformed zone volumes: σ_{ij}^n
 - ii. Calculate mass flux at ξ and η edges: $F_{i\pm 1/2,j}$, $F_{i,j\pm 1/2}$
 - iii. Calculate remapped zone mass: M_{ij}^{n+1}
 - iv. Calculate remapped zone density (Equation 1): ρ_{ij}^{n+1}
10. Calculate remapped model properties (Equation 2): w_{ij}^{n+1}
11. Assign ρ_{ij}^{n+1} and w_{ij}^{n+1} values to model zones and gridpoints
12. Apply constitutive model-specific consistency corrections
13. Continue analysis at Step 2

Acknowledgements

The authors appreciate the financial support of the National Science Foundation (award CMMI-1300518) and the California Department of Water Resources (contract 4600009751). Any opinions, findings, and conclusions or recommendations expressed in this material are those of the authors and do not necessarily reflect the views of either agency.

Notation

The following symbols are used in this paper:

δ	Interface friction ratio;
$\delta\sigma$	Transport volume;
η	Quadrilateral coordinate mapping j direction
$\Delta\eta$	η edge length;
ξ	Quadrilateral coordinate mapping i direction
$\Delta\xi$	ξ edge length;
$\Delta_{\xi}w$	ξ direction van Leer central difference limiter;
$\Delta_{\eta}w$	η direction van Leer central difference limiter;
F	Mass flux;
i	Discrete grid zone index in the ξ direction
j	Discrete grid zone index in the η direction
J	Zone Jacobian;
$K_{o\ominus}$	Coefficient of lateral earth pressure;
M	Zone mass;
N_{KT}	Cone bearing factor;
n	Discrete Eulerian time index;
\mathbf{n}^{ξ}	ξ edge normal vector;

\mathbf{n}^η	η edge normal vector;
ω_L	Van Leer limiting factor;
p	Mean total stress;
ϕ_{cone}	Cone friction angle;
ϕ'_{cs}	Soil critical state friction angle;
Q	Volume flux;
q_t	Cone penetration resistance;
ρ	Density;
\mathbf{s}	Gridpoint remapping velocity;
s_u	Undrained shear strength;
s_u/σ'_{vo}	Undrained shear strength ratio;
σ	Zone volume;
σ'_{vo}	Vertical effective stress;
t_f	Pseudo time-step for rezoning and remapping;
u	Pore water pressure;
w	General model property;
w_ξ	ξ gradient;
w_η	η gradient; and
\mathbf{X}	Gridpoint coordinates.

References

Abu-Farsakh, M. Y., Voyiadjis, G. Z., and Tumay, M. T. (1998). "Numerical Analysis of the Miniature Piezocone Penetration Tests (PCPT) in Cohesive Soils." *Int. J. Numer. Anal. Met.*, 22, 791-818.

- Abu-Farsakh, M. Y., Tumay, M. T., and Voyiadjis, G. Z. (2003). “Numerical Parametric Study of Piezocone Penetration Test in Clays.” *Int. J. Geomech.*, [10.1061/\(ASCE\)1532-3641\(2003\)3:2\(170\)](https://doi.org/10.1061/(ASCE)1532-3641(2003)3:2(170)), 170-181.
- Ahmadi, M. M., and Robertson, P. K. (2005). “Thin-Layer Effects on the CPT q_c Measurement.” *Can. Geotech J.*, 42(5), 1302-1317.
- Aubram, D., Rackwitz, F., Wriggers, P., and Savidis, S. A. (2015). “An ALE method for penetration into sand utilizing optimization-based mesh motion.” *Comput. and Geotech.*, 65, 241-249.
- Baligh, M. M. (1985). “Strain path method.” *J. Geotech. Engrg.*, [10.1061/\(ASCE\)0733-9410\(1985\)111:9\(1108\)](https://doi.org/10.1061/(ASCE)0733-9410(1985)111:9(1108)).
- Chai, J., Sheng, D., Carter, J. P., and Zhu, H. (2012). “Coefficient of consolidation from non-standard piezocone dissipation curves.” *Comput. and Geotech.*, 41, 13-22.
- Colella, P. (1990). “Multidimensional upwind methods for hyperbolic conservation laws.” *J. of Comput. Phys.*, 87, 171-200.
- Dukowicz, J. K., and Kodis, J. W. (1987). “Accurate conservative remapping (rezoning) for arbitrary Lagrangian-Eulerian computations.” *Int. J. Sci. Stat. Comput.*, 8(3), 305-321.
- Estabrook, A. H. (1991). “Comparison of recompression and SHANSEP strength-deformation properties of undisturbed Boston blue clay from automated triaxial testing.” MSc thesis, Massachusetts Institute of Technology.
- Fayad, P. H. (1986). “Aspects of the volumetric and undrained behaviour of Boston blue clay.” MSc thesis, Massachusetts Institute of Technology.
- Fleming, K., Weltman, A., Randolph, M., and Elson, K. (2009). *Piling engineering Third Edition*, Taylor & Francis, New York, New York.
- Huang, W., Sheng, D., Sloan, S. W., and Yu, H. S. (2004). “Finite element analysis of cone penetration in cohesionless soil.” *Comput. and Geotech.*, 31, 517-528.
- Itasca (2016). *FLAC – Fast Lagrangian Analysis of Continua, Version 8.0*, Itasca Consulting Group, Inc., Minneapolis, Minnesota.
- Jaeger, R. A. (2012). “Numerical and experimental study on cone penetration in sands and intermediate soils.” PhD Thesis, University of California, Davis.
- Kouretzis, G. P., Sheng, D., and Wang, D. (2014). “Numerical simulation of cone penetration testing using a new critical state constitutive model for sand.” *Comput. and Geotech.*, 56, 50-60.

Kulhawy, F. H., and Mayne, P. W. (1990). "Manual on estimating soil properties for foundation design." Research report 1493-6, Geotechnical Engineering Group, Cornell University.

Ladd, C. C., and Varallyay, J. (1965). "The influence of stress system on the behaviour of saturated clays during undrained shear." Research report R65-11, Department of Civil Engineering, Massachusetts Institute of Technology.

Ladd, C. C., and Edgers, L. (1972). "Consolidated-undrained direct simple shear tests on Boston blue clay." Research report R72-82, Department of Civil Engineering, Massachusetts Institute of Technology.

Landon, M. M. (2007). "Development of a non-destructive sample quality assessment method for soft clays." PhD Thesis, University of Massachusetts Amherst.

Liyanapathirana, D. S. (2009). "Arbitrary Lagrangian Eulerian based finite element analysis of cone penetration in soft clay." *Comput. and Geotech.*, 36, 851-860.

Liyanapathirana, D. S., Deeks, A. J., and Randolph, M. F. (2000). "Numerical modelling of large deformations associated with driving of open-ended piles." *Int. J. Numer. Anal. Met.*, 24, 1079-1101.

Lu, Q., Randolph, M. F., Hu, Y., and Bugarski, I. C. (2004). "A numerical study of cone penetration in clay." *Geotechnique*, 54(4), 257-267.

Lunne, T., Long, M., and Forsberg, C. F. (2003). "Characterisation and engineering properties of Onsoy clay. Characterisation and engineering properties of natural soils, Vol. 1, Tan, T. S., Phoon, K. K., Hight, D. W., and Leroueil, S., eds., Balkema, Rotterdam, The Netherlands: 395-427.

Mahmoodzadeh, H., Randolph, M. F., and Wang, D. (2014). "Numerical simulation of piezocone dissipation test in clays." *Geotechnique*, 64(8), 657-666.

Marti J., and Cundall, P. A. (1982). "Mixed discretization procedure for accurate solution of plasticity problems." *Int. J. Numer. Anal. Met.*, 6, 128-139.

Matsuoka, H., and Nakai, T. (1974). "Stress-deformation and strength characteristics of soil under three different principal stresses." *Proc. Japanese Soc. Civ. Engrs.*, 232: 59-70.

Moug, D. M. (2017). "Axisymmetric cone penetration model for sands and clays." PhD Thesis, University of California, Davis.

Niemunis, A., and Herle, I. (1997). "Hypoplastic model for cohesionless soils with elastic strain range." *Mech. Cohes.-Frict. Mat.*, 2(4), 279-299.

Pember, R. B., and Anderson, R. W. (2001). "Comparison of direct Eulerian Godunov and Lagrange plus remap artificial viscosity schemes." *Proc., 15th AIAA Comput. Fluid Dyn. Conf.*, Anaheim, CA 1-11.

- Pestana, J. M., and Whittle, A. J. (1999). "Formulation of a unified constitutive model for clays and sands." *Int. J. Numer. Anal. Met.*, 23, 1215-1243.
- Pestana, J. M., Whittle, A. J., and Gens, A. (2002). "Evaluation of a constitutive model for clays and sands: Part II – clay behaviour." *Int. J. Numer. Anal. Met.*, 26, 1123-1146.
- Randolph, M. F., Carter, J. P., and Wroth, C. P. (1979). "Drive piles in clay – the effects of installation and subsequent consolidation." *Geotechnique*, 29(4), 361-393.
- Seah, T. H. (1990). "Anisotropy of normally consolidated Boston blue clay." ScD Thesis, Massachusetts Institute of Technology.
- Schneider, J. A., Randolph, M. F., Mayne, P. W., and Ramsey, N. R. (2008). "Analysis of factors influencing soil classification using normalized piezocone tip resistance and pore pressure parameters." *J. Geotech. Geoenviron.*, [10.1061/\(ASCE\)1090-0241\(2008\)134:11\(1569\)](https://doi.org/10.1061/(ASCE)1090-0241(2008)134:11(1569)).
- Sheahan, T. C. (1991). "An experimental study of the time-dependent undrained shear behaviour of resedimented clay using automated stress path triaxial equipment." ScD Thesis, Massachusetts Institute of Technology.
- Su, S. F., and Liao, H. J. (2002). "Influence of strength anisotropy on piezocone resistance in clay." *J. Geotech. Geoenviron.*, [10.1061/\(ASCE\)1090-0241\(2002\)128:2\(166\)](https://doi.org/10.1061/(ASCE)1090-0241(2002)128:2(166)), 166-173.
- Susila, E., and Hryciw, R. D. (2003). "Large displacement FEM modelling of the cone penetration test (CPT) in normally consolidated soil." *Int. J. Numer. Anal. Met.*, 27, 585-602.
- Teh, C. I., and Houlsby, G. T. (1991). "An analytical study of the cone penetration test in clay." *Geotechnique*, 41(1), 17-34.
- Tolooiyan, A., and Gavin, K. (2011). "Modelling the cone penetration test in sand using cavity expansion and Arbitrary Lagrangian Eulerian finite element methods." *Comput. and Geotech.*, 38, 482-490.
- van den Berg, P., De Borst, R., and Huetink, H. (1996). "An Eulerian finite element model for penetration in layered soil." *Int. J. Numer. Anal. Met.*, 20, 865-886.
- van Leer, B. (1979). "Towards the ultimate conservative difference scheme. V. A second-order sequel to Godunov's Method." *J. Comput. Phys.*, 32, 101-136.
- Walker, J., and Yu, H. S. (2006). "Adaptive finite element analysis of cone penetration in clay." *Acta Geotech.*, 1, 43-57.
- Walker, J., and Yu, H. S. (2010). "Analysis of the cone penetration test in layered clay." *Geotechnique*, 60(12), 939-948.

Wang, D., Bienen, B., Nazem, M., Tian, Y., Zheng, J., Pucker, T., and Randolph, M. F. (2015). "Large deformation finite element analysis in geotechnical engineering." *Comput. and Geotech.*, 65, 104-114.

Yao, T. P., Sun, D. A., and Luo, T. (2004). "A critical state model for sands dependent on stress and density." *Int. J. Numer. Anal. Met.*, 28(4), 323-337.

Yi, J. T., Goh, S. H., Lee, F. H., and Randolph, M. F. (2012). "A numerical study of cone penetration in fine-grained soils allowing for consolidation effects." *Geotechnique*, 62(8), 707-719.

Yu, H. S., Herrmann, L. R., and Boulanger, R. W. (2000). "Analysis of steady cone penetration in clay." *J. Geotech. Geoenviron.*, [10.1061/\(ASCE\)1090-0241\(2000\)126:7\(594\)](https://doi.org/10.1061/(ASCE)1090-0241(2000)126:7(594)), 594-605.

Zhou, H., and Randolph, M. F. (2007). "Computational techniques and shear band development for cylindrical and spherical penetrometers in strain-softening clay." *Int. J. Geomech.*, [10.1061/\(ASCE\)1532-3641\(2007\)7:4\(287\)](https://doi.org/10.1061/(ASCE)1532-3641(2007)7:4(287)).

Table 1. Summary of direct numerical penetration work

Publication	Numerical Platform	Description of Numerical Algorithm ^a	Constitutive Model	Soil Type	Pore Water	$\delta_{\text{cone tip}}$	δ_{shaft}
Teh and Houlsby (1991)	Finite Element	Strain Path with Large Strain FE equilibrium correction	von Mises	Clay	Uncoupled-Undrained	0	0,1
van den Berg et al. (1996)	Finite Element	ALE with a static cone and fixed element nodes	Drucker-Prager	Sand & Incompressible Clay	Drained (sand); Uncoupled-Undrained (clay)	0.31 (sand) 0.67 (clay)	
Abu-Farsakh et al. (1998)	Finite Element	Large deformation finite strain from a wished in place initial condition	Modified Cam-Clay	Clay	Undrained	0, 0.25	
Yu et al. (2000)	Finite Element	Steady-state finite element analysis	Modified Cam-Clay	Clay	Undrained	0, 0.25, 0.5, 0.75, 1	
Abu-Farsakh et al. (2003)	Finite Element	Stage 1: Radial expansion to piezocone radius Stage 2: Penetration to steady state	Modified Cam-Clay	50% Kaolin 50% Fine Sand & 33% Kaolinite 67% Fine Sand	Undrained	Not Specified	
Susila & Hryciw (2003)	Finite Element	ALE with r-adaptive remeshing	Drucker-Prager	Sand	Undrained	0.48, 0.52, 0.55, 0.58, 0.61, 0.64	
Lu et al. (2004)	Finite Element	Remeshing and Interpolation Technique combined with Small Strain (RITSS)	Tresca	Clay	Undrained	0, 0.5, 1	0,1
Huang et al. (2004)	Finite Element	Finite sliding with frictional contact elements	Mohr-Coulomb	Sand	Drained	0, 0.17, 0.33, 0.5	
Ahmadi & Robertson (2005)	Finite Difference	Imposed vertical and horizontal displacement at inner boundary from a non-zero initial radius	Mohr-Coulomb	Sand & Incompressible Clay	Drained (sand); Uncoupled-Undrained (clay)	Not Specified	
Walker & Yu (2006)	Finite Element	ALE with Van Leer (1977) second order advection for remapping and adaptive remeshing with volume smoothing	von Mises	Clay	Uncoupled-Undrained	0, 0.33, 0.5, 0.67	
Liyanapathirana (2009)	Finite Element	ALE with Van Leer (1977) second order advection for remapping and adaptive remeshing with volume smoothing	von Mises	Strain softening, rate dependent clay	Uncoupled-Undrained	0, 0.33, 0.67, 1.0	
Walker & Yu (2010)	Finite Element	ALE with Van Leer (1977) second order advection for remapping and adaptive remeshing with volume smoothing	von Mises	Layered Incompressible Clay	Uncoupled-Undrained	0	
Tolooiyan & Gavin (2011)	Finite Element	ALE with volume smoothing remeshing, remapping algorithm not reported	Drucker-Prager	Sand	Drained	0.5	
Chai et al. (2012)	Finite Element	Continuous contact and deformation of the penetrating cone and ground	Modified Cam-Clay Mohr-Coulomb	Over Consolidated Clay Clayey Soil	Undrained	0.01	
Yi et al. (2012)	Finite Element	Updated Lagrangian formulation with logarithmic strains. Large deformations in the soil-cone area were addressed by changing the grid geometry with trial and error.	Drucker-Prager	Non-dilatant, homogeneous, elastic perfectly-plastic	Drained, Partially Drained & Undrained	0	
Kouretzis et al. (2014)	Finite Element	ALE with adaptive remeshing	Yao et al. (2004) ^b	Sand	Drained	0.5	
Mahmoodzadeh et al. (2014)	Finite Element	Modified Small Strain (MSS) Large Deformation Finite-Element (LDFE)	Modified Cam-Clay	Clay	Undrained	0	
Aubram et al. (2015)	Finite Element	ALE with remeshing smoothing and finite volume remapping	Niemunis and Herle (1997) ^c	Sand	Drained	0	
Wang et al. (2015)	Finite Element	RITSS EALE (Efficient Arbitrary Lagrangian Eulerian) CEL (Coupled Eulerian-Lagrangian)	Niemunis and Herle (1997) ^c	Sand	Drained	0	
This study	Finite Difference	ALE with second order remapping to steady state penetration	MIT-S1	Clay	Undrained	0.8	0.8

^a as described in publication^b Elastoplastic model for sand after the modified Cam clay model^c Hypoplastic model for sand for cyclic small strain loading

Table 2. Boston Blue Clay calibration for modified Cam clay (after Randolph, 1979)

MCC Parameter	Parameter Description	Value
λ	Slope of virgin consolidation line in $e - \ln(p')$ space	0.15
κ	Slope of unload-reload line in $e - \ln(p')$ space	0.03
ν	Poisson's ratio	0.30
v_{CSL}	Reference specific volume ($1 + e$) at $p' = 1$ on the critical state line	2.744
ϕ'_{cs}	Critical state friction angle	30°
K_{ONC}	Lateral earth pressure coefficient at normally consolidated conditions	0.49 ^a

^a changed from the Randolph (1979) calibration

Table 3. Undrained shear strength ratio (s_u/σ'_{v0}) for Boston Blue Clay specimens and single element simulations

Test	Lab Tests		Single Element Simulations		
	Intact	Resedimented	Mohr-Coulomb	Modified Cam Clay ^a	MIT-S1 ^b
OCR 1					
CK ₀ UC	0.28 ^c	0.33 ^d	0.30	0.30	0.32
CK ₀ UE	-	0.14 ^d	0.30	0.30	0.18
CK ₀ UDSS	-	0.20 ^e	0.30	0.34	0.17
OCR 2					
CK ₀ UC	0.42 ^c	0.54 ^g	0.55	0.55	0.52
CK ₀ UE	0.28 ^f	0.31 ^h	0.55	0.55	0.34
CK ₀ UDSS	-	0.32 ⁱ	0.55	0.62	0.35
OCR 2.2					
CK ₀ UC	0.45 ^c	-	0.59	0.59	0.54
CK ₀ UE	-	-	0.59	0.59	0.38
CK ₀ UDSS	-	-	0.59	0.67	0.36

^aRandolph et al. (1979)

^eSeah (1990)

ⁱLadd & Edgers (1972)

^bJaeger (2012)

^fEstabrook (1991)

^cLandon (2007)

^gSheahan (1991)

^dLadd & Varallyay (1965)

^hFayad (1986)

Table 4. Boston Blue Clay calibration for MIT-S1

MIT-S1 Parameter	Parameter Description	Value
ρ_c	Slope of virgin compression curve in $\log(e) - \log(p')$ space	0.178
p'_{ref}/p_{atm}	Reference p' at $e = 1$ on the isotropic virgin compression curve	1.5
θ	Controls transition to limiting compression curve ($\theta = 0$ for clays)	0.0
D	Characterizes slope of unloading curve	0.04
r	Characterizes shape of unloading curve	0.30
K_{ONC}	Lateral earth pressure coefficient at normally consolidated conditions	0.49
μ'_o	Small strain Poisson's ratio	0.24
ω	Controls non-linearity in Poisson's ratio	1.0
C_b	Controls small strain elastic moduli.	850.0
ϕ'_{cs}	Critical state friction angle	33.5
ϕ'_{mr}	Peak friction angle at $e = 1$	46.0
p_ϕ	Controls variation of peak friction angle with void ratio ($p_\phi = 0$ for clays)	0.0
m	Controls shape of yield and bounding surfaces	0.80
ω_s	Controls non-linearity of elastic moduli in shear	8.0
ψ	Controls rate of evolution of the yield surface anisotropy	8.0
h	Controls plastic strain magnitude when $OCR > 1$	6.0

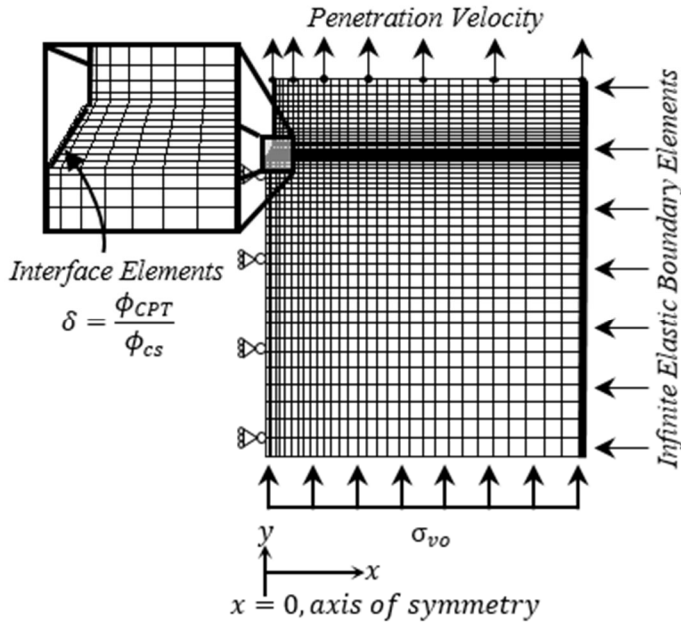


Fig. 1. Direct axisymmetric penetration model geometry and boundary conditions

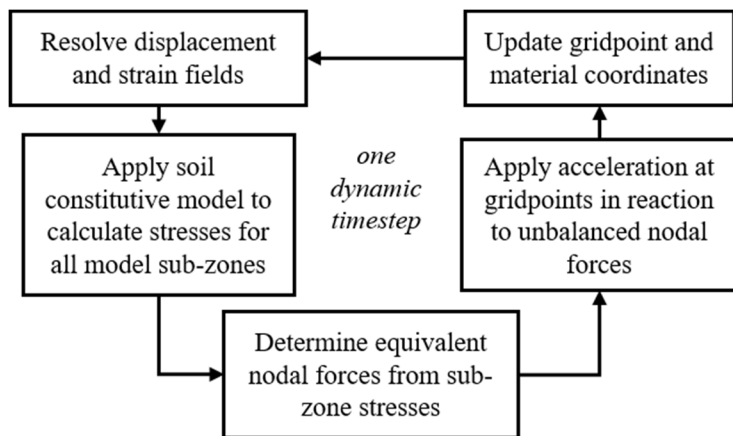


Fig. 2. FLAC mechanical calculation cycle

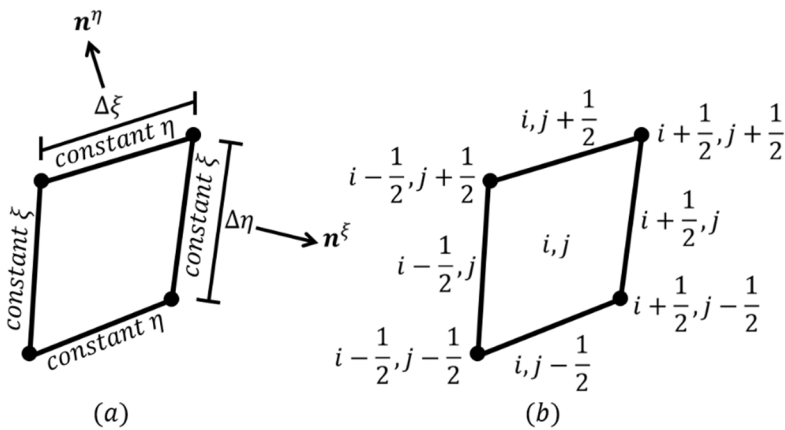


Fig. 3. (a) Quadrilateral grid convention, and (b) index space coordinates for ALE algorithm

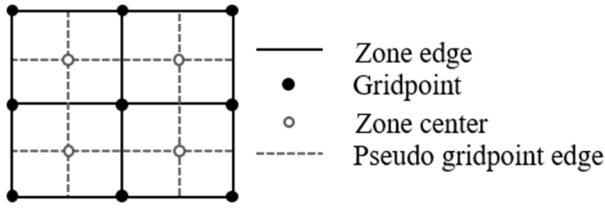


Fig. 4. Pseudo gridpoint edge values for gridpoint value remapping

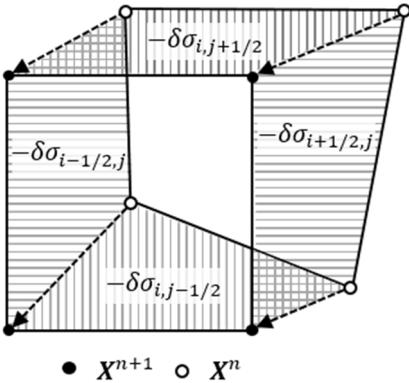


Fig. 5. Volume fluxes during the rezoning step and the Eulerian remapping interval

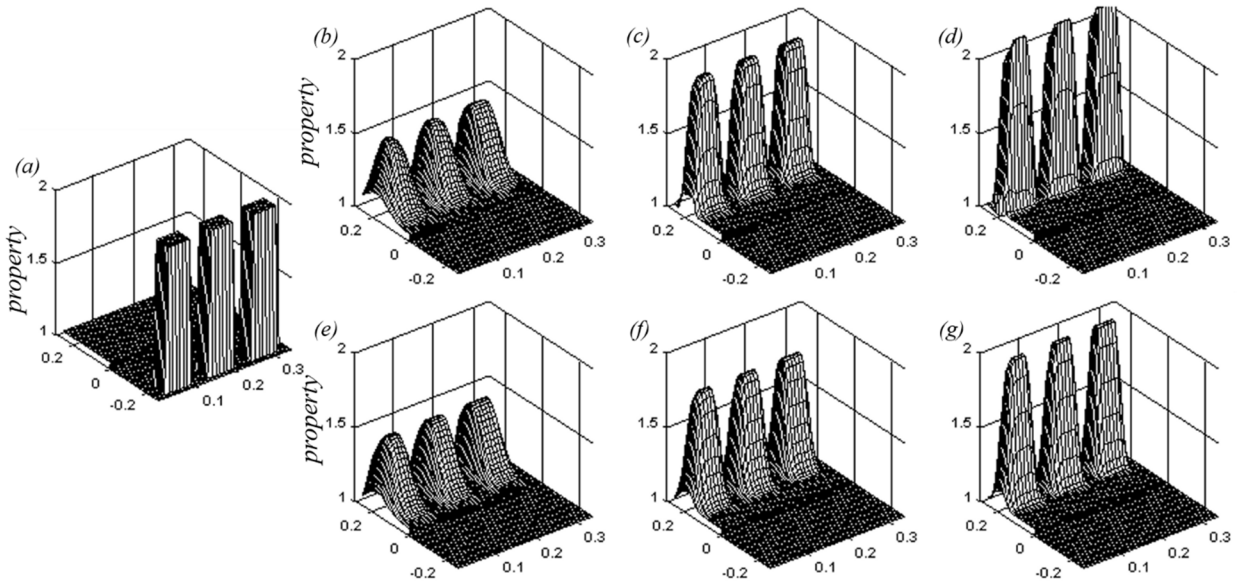


Fig. 6. (a) Initial property distribution, (b) 500 remapping steps with limiting factor = 0, (c) 500 remapping steps with limiting factor = 1, (d) 500 remapping steps with limiting factor = 2, (e) 5000 remapping steps with limiting factor = 0, (f) 5000 remapping steps with limiting factor = 1, and (g) 5000 remapping steps with limiting factor = 2

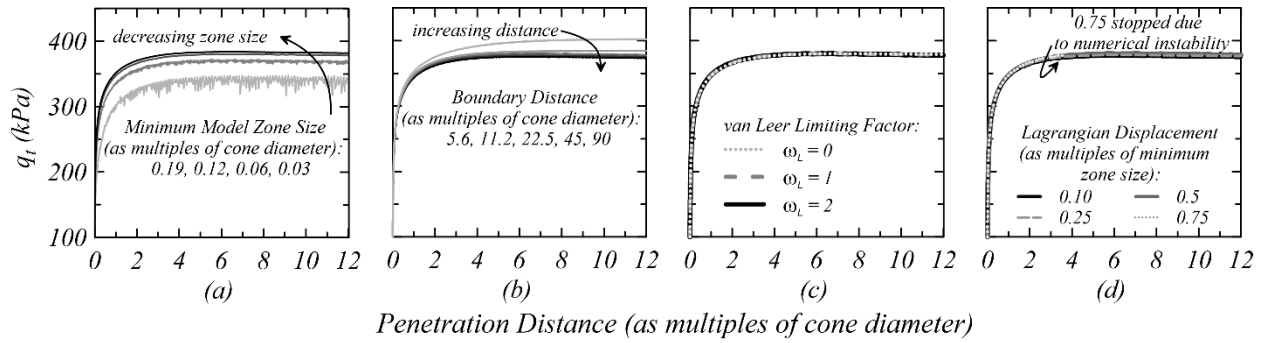


Fig. 7. Direct penetration model verification for (a) model zone size, (b) model boundary distance, (c) van Leer limiting factors, and (d) Lagrangian displacement interval

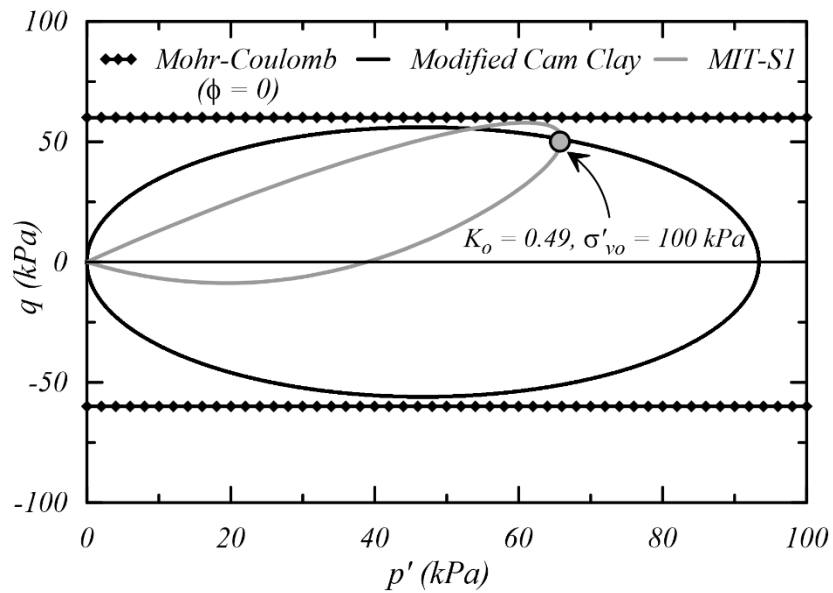


Fig. 8. Yield surfaces for K_o normally consolidated BBC with Mohr-Coulomb, modified Cam clay, and MIT-S1 constitutive models

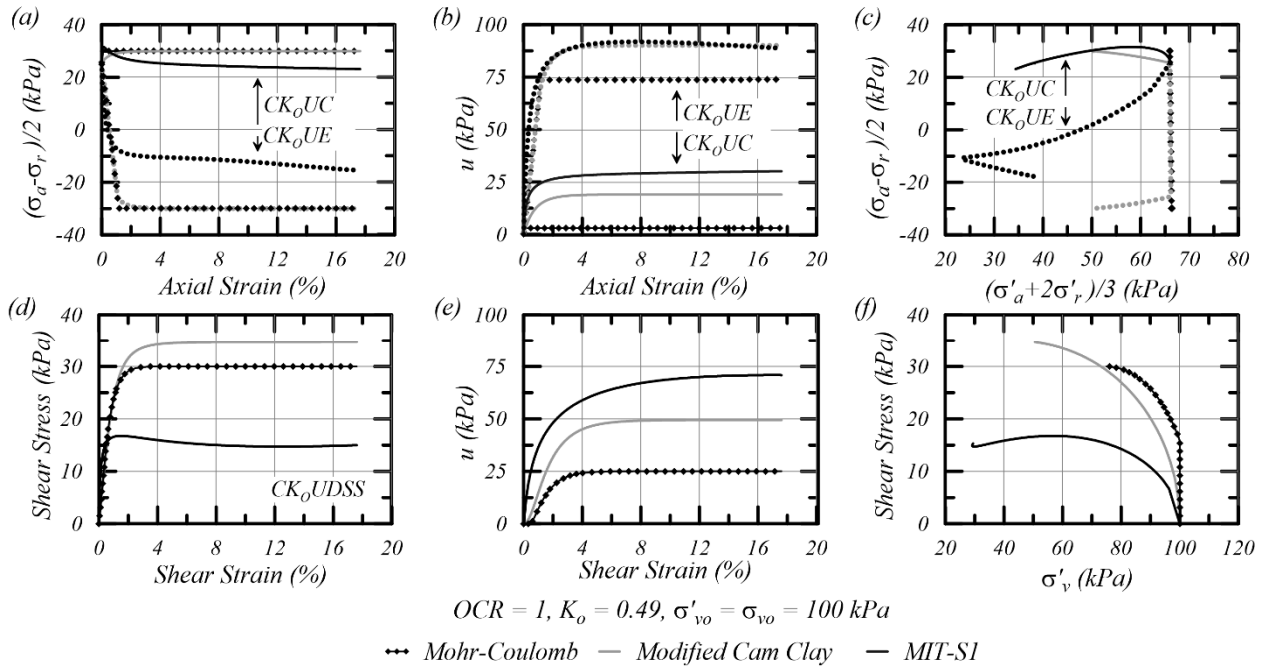


Fig. 9. Single element simulations for normally consolidated BBC with MC, MCC, and MIT-S1 constitutive models: (a-c) CKoUC and CKoUE loading, and (d-f) CKoUDSS loading

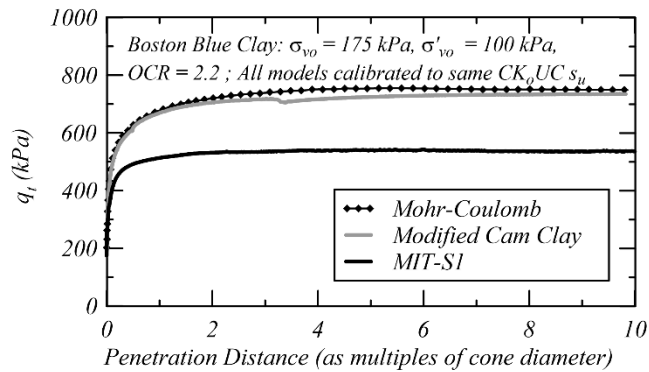


Fig. 10. Simulated cone tip resistance versus penetration distance in BBC

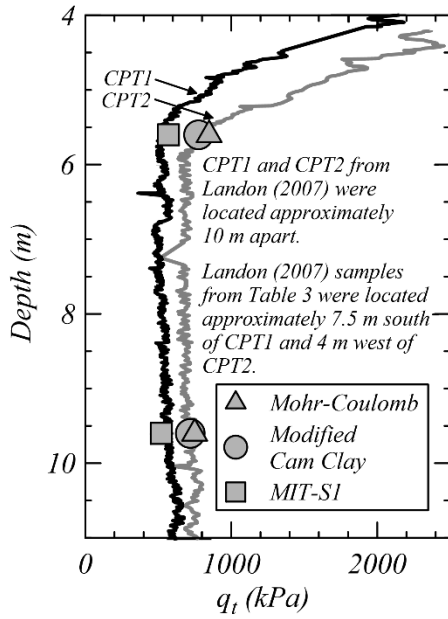


Fig. 11. CPT profiles in BBC at Newbury, MA and simulated cone tip resistance at 5.6 and 9.6 m below ground surface (bgs)

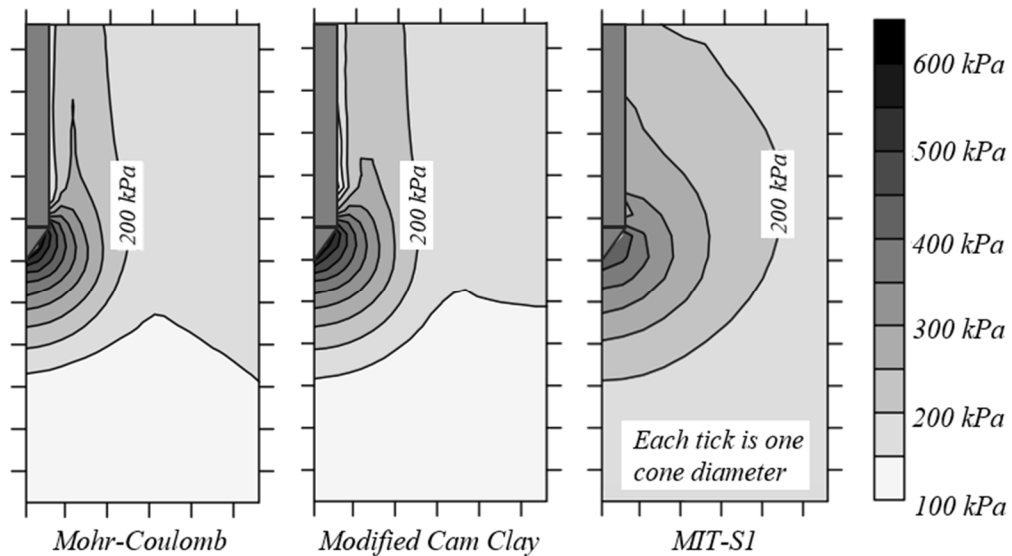


Fig. 12. Total mean stress distribution at 25 CPT diameters of penetration in BBC

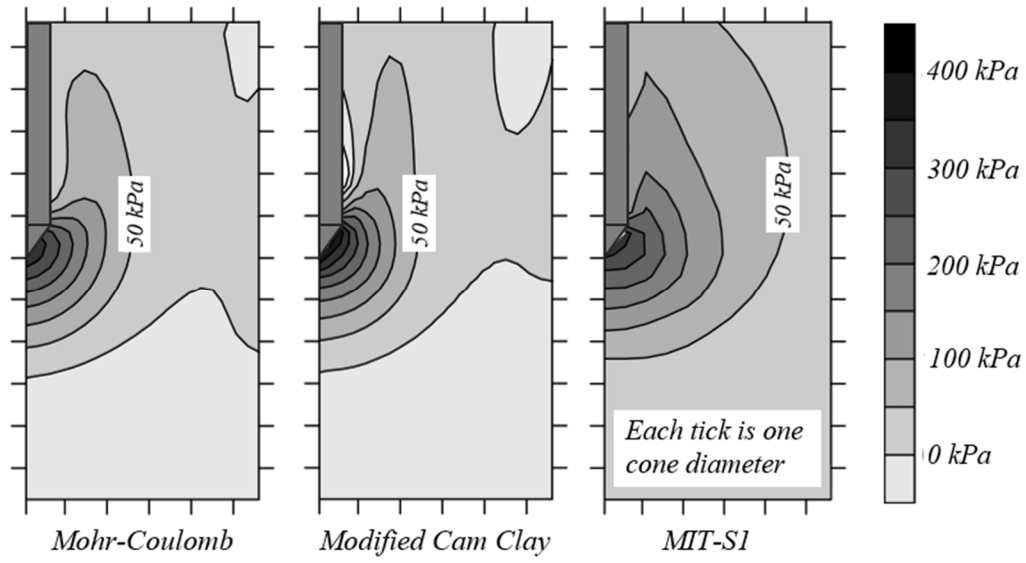


Fig. 13. Excess pore pressure distribution at 25 CPT diameters of penetration in BBC